Computer Modeling in Engineering & Sciences CMES, vol.123, no.3, pp.1105-1129, 2020

Safety Performance of a Precast Concrete Barrier: Numerical Study

Zishen Li[1], Xiangling Gao[1, *] and Zicheng Tang[2]

Abstract: The numerical simulation for a new type of precast concrete barrier for viaducts is carried out systematically. To obtain an accurate representation of the damage state of the concrete barrier under the impact of a vehicle, a stochastic damage-plasticity model of the concrete is adopted in the finite element model. Meanwhile, a simplified mathematical model of the impact between vehicles and the concrete barrier was established and the input energy was converted to the impact load to facilitate the investigation of the safety performance of the concrete barriers. On this basis, a refined finite element (FE) model of a precast concrete barrier was developed. The impact locations, impact load, boundary constraints, and reinforcement types were used as variables and the dynamic response of the precast concrete barrier was systematically analyzed under 36 working conditions. The simulated results indicated that the damage state of the concrete barrier and the stress of the reinforcing bars were accurately and quantitatively reflected. According to the computed results, some suggestions were put forward for selecting the appropriate reinforcement type of the precast concrete barrier and the connection between the superstructure and foundation.

Keywords: Concrete barrier, numerical simulation, safety performance, stochastic damage-plasticity model, dynamic response, damage state.

1 Introduction

Roadside barriers with high safety requirements can significantly reduce traffic accidents and minimize economic losses. At present, barrier systems include concrete barriers, W-beam guardrails, and cable barriers. Concrete barriers have excellent anti-collision performance, low cost, and almost no maintenance [Kusama (2004)] and their dynamic deformation is much lower than that of the other two types of barriers. For this reason, concrete barriers are widely used on highways and viaducts with a large traffic volume of medium and large-sized vehicles. However, since the concrete barrier has to absorb the

[1] College of Civil Engineering, Tongji University, Shanghai, 200092, China.
[2] Green Science Architecture Industry Development Co., Ltd., Guiyang, 551400, China.
* Corresponding Author: Xiangling Gao. Email: gaoxl@tongji.edu.cn.
Received: 08 November 2019; Accepted: 10 March 2020.

energy of impacts and to prevent vehicles from overturning after an impact, its shape and size have to meet strict requirements. Thus, the cast-in-situ concrete barriers have long construction period for the complex installation. In contrast, when precast concrete barriers are used, the construction speed is relatively fast, the quality is high, and the costs are low.

Researchers have extensively used full-scale impact tests to analyze and evaluate the safety performance of various barrier systems since the NCHRP Report 350 was adopted as the first formal safety standard for roadside barriers [Ross, Sicking, Zimmer et al. (1993)]. The safety of W-beam guardrails has been improved as a result of a large number of experimental studies [Reid, Sicking, Faller et al. (1997); Sicking, Reid and Rohde (2002); Atahan and Cansiz (2005); Ren and Vesenjak (2005); Faller, Sicking, Bielenberg et al. (2007); Faller, Reid, Kretschmann et al. (2009); Soltani, Moghaddam, Karim et al. (2013)]. In addition, Ahmed et al. [Ahmed, Dulude and Benmokrane (2013)] verified the feasibility of the MTQ 311 reinforced concrete barrier system through experimental research. Even though full-scale impact tests are irreplaceable for determining the compliance of a barrier system to the safety standard, these tests are in practice too expensive. Since the invention of the finite element method (FEM) in the 1950s, FEM has become the most popular method in engineering computations [Li and Liu (2002)] FEM can be used to analyze the anti-impact performance of unconstrained glass plate and energy absorbing system made of high performance concrete, and the simulation results were very close to the test results [Hála, Sovják, Frydrýn et al. (2017); Janda, Zemanová, Hála et al. (2020)]. Currently, commercial software such as LS-DYNA and ABAQUS has become a widely used analysis method to simulate vehicular crashes.

The design of the concrete barrier has been continuously innovated. A large number of finite element (FE) analyses have been conducted to simulate vehicular crashes and the results were compared with full-scale test results to verify the feasibility of the FE method [Consolazio, Chung and Gurley (2003); Bligh, Sheikh, Menges et al. (2005); Deb, Naravane and Chirwa (2006); Itoh, Liu and Kusama (2007); Jeon, Choi and Kim (2008); Atahan (2006, 2009); Borkowski, Hryciów, Rybak et al. (2011); Mohammed and Zain (2016); Kim, Lee, Kim et al. (2019); Sennah and Hedjazi (2019)].

In addition, Borkowski et al. [Borkowski, Hryciów, Rybak et al. (2010)] simulated vehicles crashing into a barrier and found that the connection between the barrier and the foundation had a significant impact on the collision process and the dynamic loads affecting the car passengers. Based on the results of the NCHRP Report 350, Marzougui et al. [Marzougui, Kan and Opiela (2012)] investigated the impact of road curvature on the anti-collision performance of concrete barriers using numerical simulation. Bielenberg et al. [Bielenberg, Faller, Reid et al. (2018)] developed a reinforced structure to reduce the deformation deflection of an F-shaped portable concrete barrier system and the validity of the proposed structure was demonstrated using LS-DYNA.

Due to the high cost of a full-scale impact test, numerical simulations have significant advantages for parameter optimization of barrier systems. Zhao et al. [Zhao, Lei, Wang

et al. (2011)] conducted FE analysis on 25 sets of concrete barriers with different cross-sectional parameters and obtained the optimal solution using SPSS analysis. Hou et al. [Hou, Zheng, Xie et al. (2014)] used a multi-island genetic algorithm to optimize the total height, slope height, and climbing angle of an NJ-shaped guardrail. Yin et al. [Yin, Fang, Wang et al. (2016)] optimized the parameters of concrete barriers by combining nonlinear FE simulation, metamodeling with radial basis functions, and a genetic algorithm. Pachocki et al. [Pachocki and Wilde (2018)] conducted a parametric analysis of concrete barriers and compared the simulation results with the results of full-scale impact tests; a database of concrete barriers under various initial conditions was established. However, previous numerical simulation analyses of concrete barriers generally used a single type of vehicle to impact the barrier, and the FE model of the specific vehicle was the focus of previous analyses. Thus, those FE model of the barrier was relatively coarse and failed to reflect the dynamic response of the barrier when different types of vehicles collide with it.

The collision between a vehicle and the barrier is a system dynamics problem that can be solved by using an explicit time integration algorithm, which is one of two direct integration algorithms used in transient dynamics analysis [Ma, Kong and Jin (2018)]. Lai et al. [Lai, Ren, Fan et al. (2015)] developed nonlinear peridynamics models to simulate the geomaterial fragmentation under impulse loads. In addition, ABAQUS software has a mature explicit solution module that accurately simulates the expansion of elastoplastic cracks [Liang, Ren and Li (2015); Ren, Liu, Li et al. (2017); Wang, Jiang and Wang (2019)]. Therefore, the ABAQUS software is used in this study to establish and refine a suitable FE model of a precast barrier and a comparative analysis of the simulation results is performed. On this basis, a general nonlinear full-process numerical analysis and simulation scheme for precast concrete barriers is proposed by using the stochastic damage-plasticity model of concrete and comprehensive evaluation results are provided for the performance of a new type of precast concrete barrier.

2 Design scheme of precast concrete barrier

A new design scheme of an SS-grade precast concrete crash barrier is proposed, as shown in Fig. 1; the barrier was designed according to the specifications [JTG D81-2017] and [JTG/T D81-2017]. The SS-grade of the barrier for expressways has a design speed of 120 km/h for the vehicle and when the vehicle driving out of the barriers will cause a major accident once again. The SS-grade is the highest grade of the barrier system, and it can withstand large vehicle impact loads.

The new type of precast concrete barrier system shares the same outer shape and dimension with the cast-in-situ barrier. The vertical reinforcement of the barrier includes two configuration schemes of ⌀16@100 and ⌀25@200, where ⌀16@100 is the configuration form of vertical reinforcement commonly used in an SS-grade cast-in-place concrete barrier. However, for the same volumetric reinforcement ratio, the configuration scheme ⌀25@200 has a higher vertical reinforcement spacing, which makes it more convenient

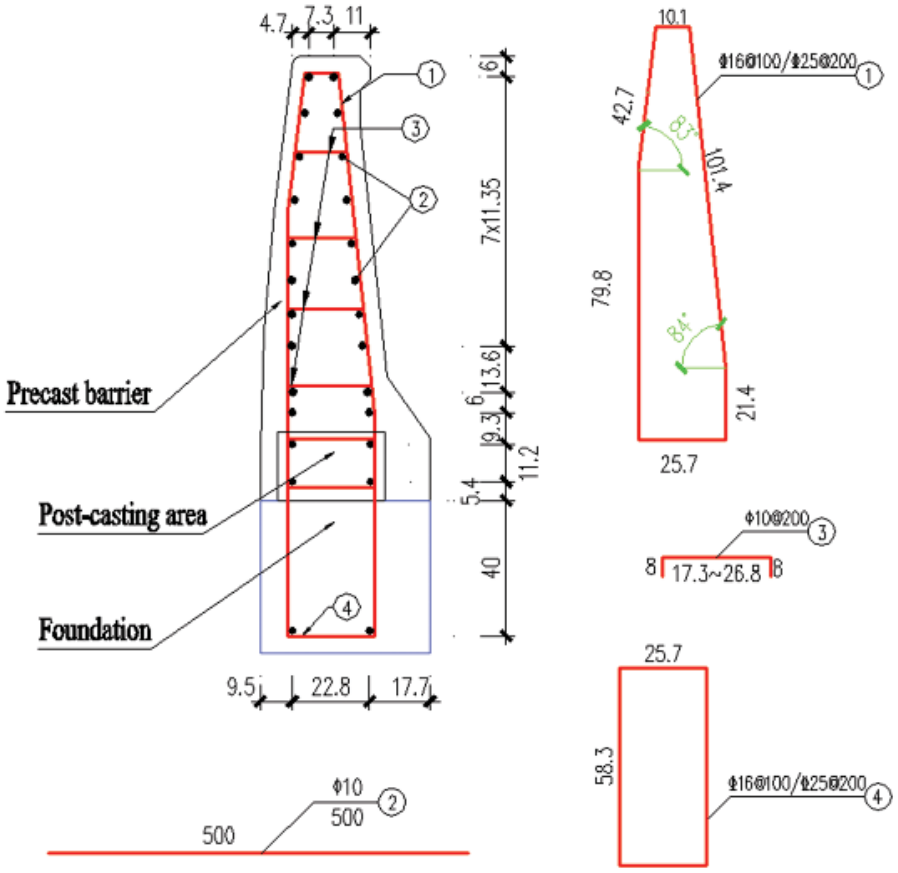

Figure 1: Diagram of the reinforcement of a precast concrete barrier

for the construction of a precast concrete barrier. As is shown in Fig. 1, the reinforcements of the precast concrete barrier are attached to the rectangular hoops on the foundation and are then joined in the post-casting area by cast-in-place concrete. Concrete with C35 grade is used for the precast concrete barrier component, the foundation, and the post-casting area.

In the actual construction, when precast barrier is put on the foundation, high-strength mortar is poured in the contact surface to fix the precast barrier on the foundation. Moreover, the hollow preset in the precast barrier (i.e., the post-pouring area as shown in Fig. 1) was poured by concrete. Finally, the precast barrier, the foundation and the post-pouring mortar constituted a complete anti-collision system. Therefore, the actual connection mode between precast barrier and foundation is equivalent to cast-in-place under ideal conditions.

3 Finite element model of precast concrete barrier

3.1 Constraints and boundary conditions

3.1.1 Constraints

Numerical simulation analysis of the precast concrete barriers was conducted using ABAQUS software. In order to accurately simulate the pouring sequence of different components of the precast concrete barrier system, in the FE model, the mutual relationship between the three parts were be set according to the actual working conditions. Specifically, the precast barrier components and the post-casting area were merged to form the superstructure. Then, two different types of connection were considered between the superstructure and the foundation:

(1) The contact surfaces in the cross-section of the foundation are totally merged, as shown in Fig. 2(a), which indicates that the precast barrier component is well connected with the foundation and the post-casting area. The superstructure and the foundation from one unit to jointly resist the impact load.

(2) The bottom surface of the post-casting area is attached to the corresponding position on the top surface of the foundation, as shown in Fig. 2(b), which indicates that the superstructure and the foundation are only connected in the post-casting area and there is no connection on either side of the post-casting area because the thickness of the precast barrier's bottom is relatively small. This case is used to simulate a less favorable connection between the superstructure and the foundation where the post pouring mortar connection in the contact surface between the precast barrier and the foundation may not achieve the ideal bonding state, which may weaken the connection between the barrier and the foundation.

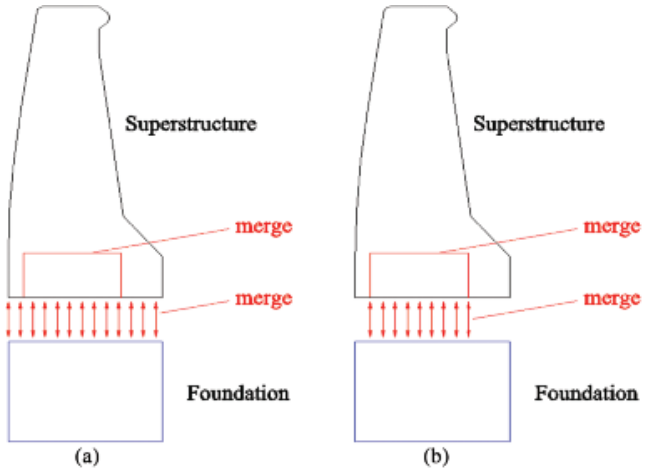

Figure 2: Constraint between superstructure and foundation. (a) Merge constraint (b) Tie constraint

3.1.2 Boundary conditions

The boundary constraints of the precast barrier system are determined for actual working conditions. The degrees of freedom of the longitudinal deformation of each surface of the foundation are restricted. Two boundary conditions of the longitudinal ends of the superstructure are considered:

(1) Considering the practical conditions of a tight connection between the adjacent barriers, the longitudinal deformation of the barrier will be restricted by the adjacent barriers so that a hinge constraint at both end surfaces is adopted for restricting the longitudinal deformation at the end of the barrier.

(2) Considering the practical conditions of large gaps and no connections between the adjacent barriers, there is no interaction between the adjacent barriers. Therefore, no connection without a freedom constraint is adopted in this case.

To sum up, according to the boundary conditions and constraints, the FE models of the precast barrier include the following three types of boundary constraints: (1) merge-hinge constraint, which is the ideal constraint condition; (2) tie-hinge constraint, which is a less favorable condition; (3) tie-free constraint, which is the unfavorable condition.

3.2 Element definition and meshing

In the FE analysis, the T3D2 truss element is used for the steel bars and the C3D8R solid element is adopted for concrete and the reinforcement mesh is embedded into the solid concrete elements. The longitudinal length of the precast barrier is 5 m and the element size is 60 mm in this FE model. There are 13528 elements in total, including 1338 T3D2 truss elements and 12200 C3D8R solid elements. Fig. 3 shows the reinforcement mesh models of the two types of reinforcements. Fig. 4 depicts the mesh of the FE element model of the precast concrete barrier according to the design scheme shown in Fig. 1.

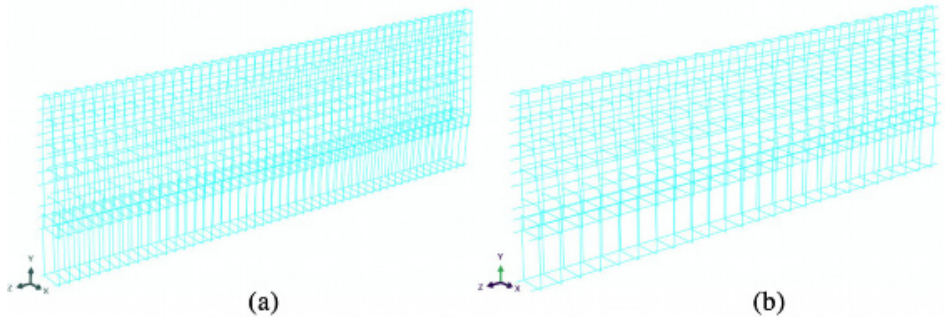

Figure 3: Schematic diagram of the reinforcement mesh of the precast barrier. (a) Vertical reinforcement of ⌀16@100 (b) Vertical reinforcement of ⌀25@200

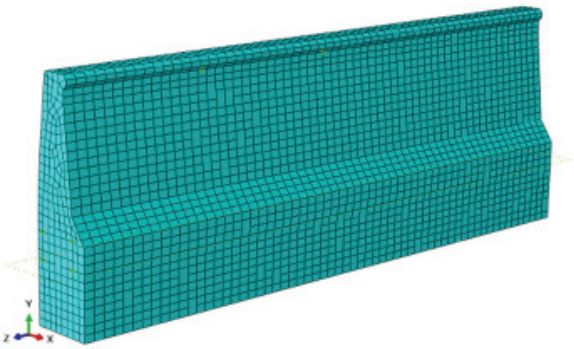

Figure 4: Schematic diagram of the mesh division of the FE model of the precast barrier

3.3 Constitutive models of the materials

3.3.1 Constitutive model of the steel bars

The constitutive model of the steel bars is based on a bilinear kinematic hardening model, as shown in Fig. 5. For the vertical reinforcement, the yield strength f_y is 400 MPa; the ultimate tensile strength f_u is 540 MPa; the elastic modulus E_s is 200 GPa; the yield strain ε_y is 0.002; the ultimate strain ε_u is 0.072. For the horizontal reinforcement and tensile reinforcement, f_y is 300 MPa, f_u is 420 MPa, E_s is 200 GPa, ε_y is 0.0015, and ε_u is 0.0615.

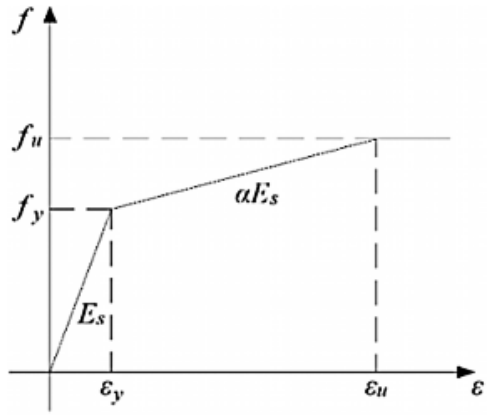

Figure 5: Constitutive model of the steel bars

3.3.2 Constitutive model of concrete

Due to the need for a refined analysis of the precast concrete barrier system, the stochastic damage-plasticity model of concrete proposed by Li et al. [Li and Ren (2009); Ren, Zeng and Li (2015)] is used to simulate the damage development of the concrete under an impact load. The detailed derivation can be found in these literatures and only the main

formula was given here. In this constitutive model, the strain of concrete ε was decomposed into two components that are elastic strain $\boldsymbol{\epsilon}^{\mathrm{e}}$ and plastic strain $\boldsymbol{\epsilon}^{\mathrm{p}}$.

$$\boldsymbol{\varepsilon}=\boldsymbol{\varepsilon}^{\mathrm{e}}+\boldsymbol{\varepsilon}^{\mathrm{p}} \tag{1}$$

Within the framework of irreversible thermodynamics, an elastoplastic damage theory should be established based on Helmholtz free energy (HFE) potential. And the total HFE potential can be defined as the sum of the elastic component ψ^{e} and the plastic component ψ^{p}, that is

$$\psi(\boldsymbol{\varepsilon}^{\mathrm{e}}, \boldsymbol{\kappa}^{\mathrm{p}}, d^{+}, d^{-})=\psi^{\mathrm{e}}(\boldsymbol{\varepsilon}^{\mathrm{e}}, d^{+}, d^{-})+\psi^{\mathrm{p}}(\boldsymbol{\kappa}^{\mathrm{p}}, d^{+}, d^{-}) \tag{2}$$

where, $\boldsymbol{\kappa}^{\mathrm{p}}$ denotes a suitable set of plastic variables; d^{+} and d^{-} denote the tensile and compressive damage scalar respectively.

The damage process and plastic flow process of materials are both irreversible thermodynamic processes. According to the second principle of thermodynamics, any irreversible process must satisfy the Clausius-Duheim inequality, and thus the damage constitutive relationship of concrete can be deduced.

$$\begin{aligned}\boldsymbol{\sigma} &= (1-d^{+})\frac{\partial \psi_0^{\mathrm{e}+}}{\partial \boldsymbol{\varepsilon}^{\mathrm{e}}}+(1-d^{-})\frac{\partial \psi_0^{\mathrm{e}-}}{\partial \boldsymbol{\varepsilon}^{\mathrm{e}}} \\ &=(1-d^{+})\bar{\boldsymbol{\sigma}}^{+}+(1-d^{-})\bar{\boldsymbol{\sigma}}^{-}=(\mathbf{I}-\mathbf{D}):\bar{\boldsymbol{\sigma}}=(\mathbf{I}-\mathbf{D}):\mathbf{C}_0:\boldsymbol{\varepsilon}^{\mathrm{e}}\end{aligned} \tag{3}$$

where, $\bar{\boldsymbol{\sigma}}$ is the effective stress tensor, and $\mathbf{C}_0$ is a fourth order tensor denoting the initial undamaged elastic stiffness.

Therefore, the damage evolution under multi-dimensional stress can be obtained by directly substituting the energy equivalent strain into the one-dimensional damage evolution. In this study, the tensile damage variable d^{+} of concrete is expressed by Eq. (4). When d^{+} is close to 1.0, it indicates that the corresponding concrete has undergone severe tensile cracking.

$$d^{+}=\begin{cases} 1-\rho_t[1.2-0.2x^5], & x\le 1 \\ 1-\dfrac{\rho_t}{\alpha_t(x-1)^{1.7}+x}, & x>1 \end{cases} \tag{4}$$

$$x=\frac{\varepsilon_{\mathrm{eq}}^{+}}{\varepsilon_{t,r}} \tag{5}$$

$$\rho_t=\frac{f_{t,r}}{E_c\varepsilon_{t,r}} \tag{6}$$

where α_t is the parameter of the descending section of the uniaxial tensile stress-strain curve; $f_{t,r}$ is the representative value of the uniaxial tensile strength; $\varepsilon_{t,r}$ is the peak uniaxial tensile strain; and ε_{eq}^{+} is the energy equivalent tensile strain.

The compressive damage variable d^- of concrete can be expressed by Eq. (7). When d^- is close to 1.0, it indicates that the corresponding concrete has undergone severe compressive failure.

$$d^- = \begin{cases} 1 - \dfrac{\rho_c n}{n - 1 + x^n}, & x \le 1 \\ 1 - \dfrac{\rho_c}{\alpha_c (x-1)^2 + x}, & x > 1 \end{cases} \tag{7}$$

$$x = \frac{\varepsilon_{\mathrm{eq}}^-}{\varepsilon_{c,r}} \tag{8}$$

$$\rho_c = \frac{f_{c,r}}{E_c \varepsilon_{c,r}} \tag{9}$$

$$n = \frac{E_c \varepsilon_{c,r}}{E_c \varepsilon_{c,r} - f_{c,r}} \tag{10}$$

where, α_c is the parameter of the descending section of the uniaxial compressive stress-strain curve; $f_{c,r}$ is the representative value of the uniaxial compressive strength; $\varepsilon_{c,r}$ is the peak uniaxial compressive strain; and ε_{eq}^- is the energy equivalent compressive strain.

This model gives a reasonable explanation for the damage evolution law of concrete on the physical mechanism, and has been maturely applied to the nonlinear analysis of concrete structures [Li, Feng, Ren et al. (2017); Feng, Yang and Ren (2018)]. The precast barrier, post-casting area, and the foundation all consist of concrete with the strength grade of C35, whose elastic modulus is 31,500 MPa, the Poisson's ratio is 0.2, the compressive strength is 23.4 MPa, and the tensile strength is 2.2 MPa.

3.4 Load value

According to the vehicle impact area on the barrier, two conditions are considered, namely a central impact or a corner impact. The precast concrete barrier designed in this study is SS-grade. According to references [JTG D81-2017] and [JTG/T D81-2017], the location of the impact point is 1.22 m from the road surface and the length over which the load is distributed is 2.4 m in the middle for central impact and at the left upper corner for corner impact as shown in Fig. 6. The standard value of the impact load P_k is 520 kN and the loading time is 0.1 s. The value of 520 kN was the maximum lateral impact force in the simplified mathematical model [JTG D81-2017]. And 0.1 s is the time when the vehicle crashes the rigid barrier considered in the specification [JTG D81-2017]. In addition, the crash time 0.1 s was also used to study the collision process by many researchers [Ahmed, Dulude and Benmokrane (2013); Borkowski, Hryciów, Rybak et al. (2010); Jiang, Grzebieta and Zhao (2004)]. However, in extreme cases, the impact load of the vehicle needs to be multiplied by the power amplification factor of 1.8. In order to examine the anti-collision performance of the new precast concrete barrier system, three load conditions of 1.0 P_k, 1.4 P_k, and 1.8 P_k are considered in this numerical simulation analysis.

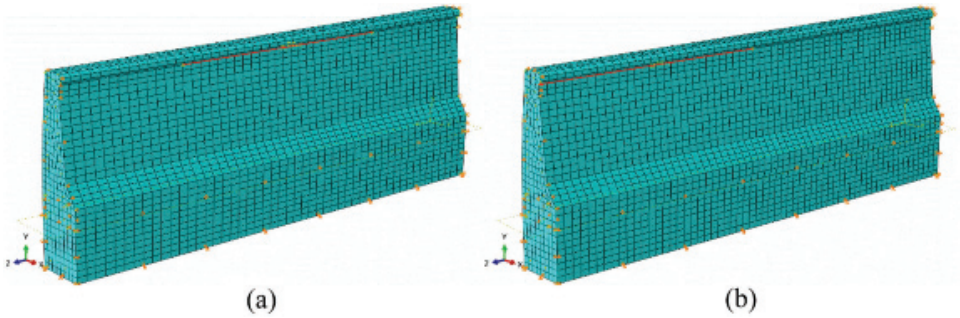

Figure 6: Schematic diagram of the location of impact load. (a) Central impact (b) Corner impact

4 Numerical analysis results

The variables considered in the numerical simulation are listed in Tab. 1 and include 2 types of vertical steel bars, 3 boundary conditions, 2 impact positions, and 3 load values. Significantly, the hinge constraint only constrains the degree of freedom of the longitudinal deformation. Therefore, according to the combination of the variables, a total of 36 working conditions need to be analyzed.

Table 1: Variables of the barrier considered in the simulation

Variable category	Variable
Impact load	1.0 P_k, 1.4 P_k, 1.8 P_k
Impact location	Central impact, Corner impact
Boundary conditions	Merge-hinge, Tie-hinge, Tie-free
Reinforcement	⌀16@100, ⌀25@200

4.1 Conditions with an impact load of 1.0 P_k

4.1.1 Central impact

The simulation results for the barrier being subjected to a central impact of 1.0 P_k (520 kN) are shown in Figs. 7 and 8. The stress contours of the steel bars are shown in Fig. 7 and the unit of stress is MPa. Fig. 8 shows the tensile damage contours of the concrete. If the damage value is close to 1, the concrete has been cracked. The numerical simulation results show the following:

(1) As shown in Figs. 7(a), 7(c), and 7(e) and Figs. 7(b), 7(d), and 7(f), the constraints at both ends of the barrier have less of influence on the stress state of the steel bars than the connection between the superstructure and foundation because the longitudinal deformation at both ends of the barrier is small. The reinforcement has not yielded under any boundary constraints.

(2) Figs. 8(a), 8(c), and 8(e) show that the concrete at the bottom of the impact zone has some tensile damage for the vertical reinforcement of ⌀16@100. For the vertical

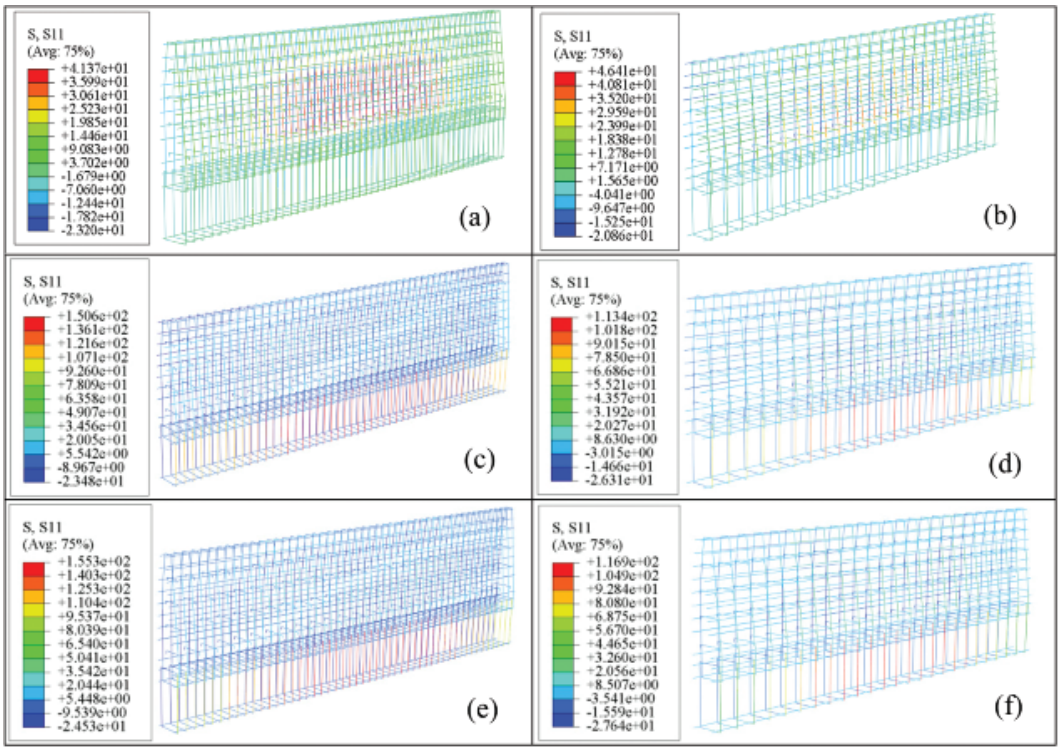

Figure 7: Stress contours of steel bars under a central impact of 1.0 P_k (a) merge-hinge, (b) merge-hinge, (c) tie-hinge, (d) tie-hinge, (e) tie-free, (f) tie-free

reinforcement of ⌀25@200 (Figs. 8(b), 8(d), and 8(f)), the overall trend of the dynamic response under the different conditions is similar but there is less tensile damage. None of the barriers has overturned and all barriers meet the requirements.

4.1.2 Corner impact

When the barriers are subjected to a corner impact of 1.0 P_k (520 kN), the tensile damage contours of the concrete under different constraint conditions are shown in Fig. 9. The barriers did not overturn under any of the six conditions. And the tensile damage of the concrete with reinforcement of ⌀25@200 is less than that with reinforcement of ⌀16@100.

4.2 Conditions with an impact load of 1.4 P_k

4.2.1 Central impact

When the barrier is subjected to a central impact of 1.4 P_k (728 kN), the tensile damage contours of the concrete are shown in Fig. 10. Under all three boundary conditions, the barriers have not overturned and the concrete at the bottom of the barrier in the impact zone suffered more serious tensile damage than that subjected to the central impact of 1.0 P_k. All six barriers meet the requirements.

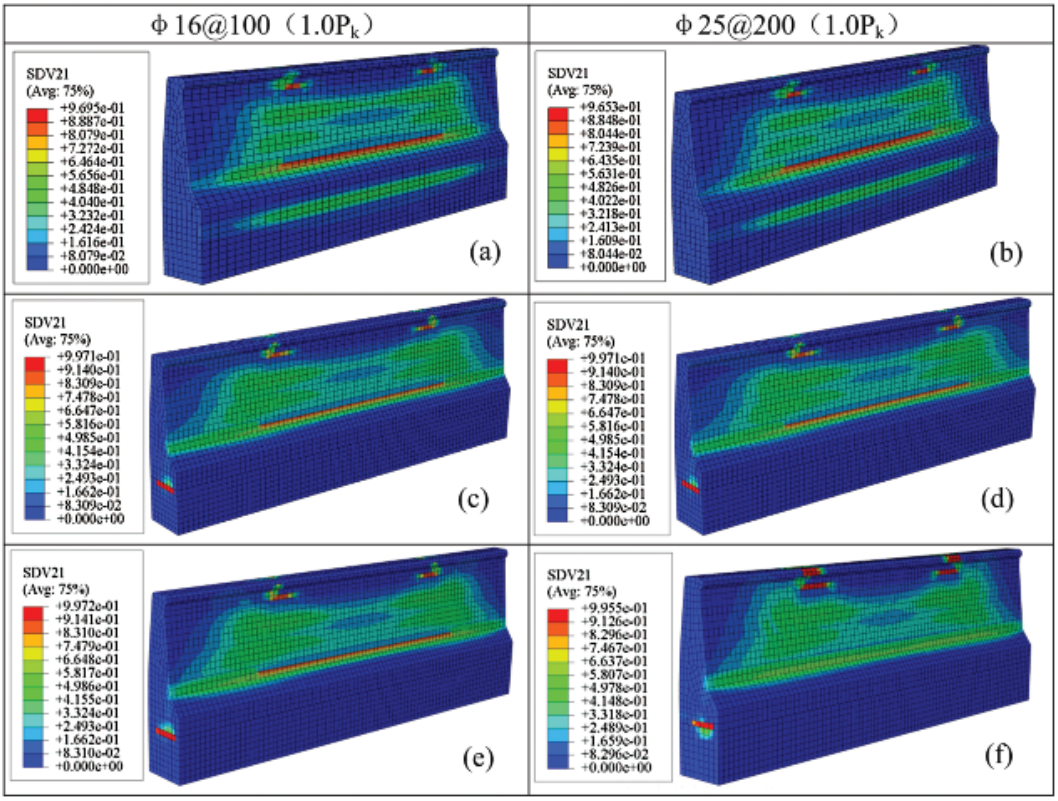

Figure 8: Tensile damage contours of concrete under a central impact of 1.0 P_k (a) merge-hinge, (b) merge-hinge, (c) tie-hinge, (d) tie-hinge, (e) tie-free, (f) tie-free

4.2.2 Corner impact

The stress contours of the steel bars and the tensile damage contours of the concrete under different conditions and a corner impact of 1.4 P_k are shown in Figs. 11 and 12, respectively.

When the barrier is reinforced with vertical reinforcement of ⌀16@100 (Fig. 11(a)), the reinforcement does not yield under ideal conditions. Under less favorable conditions, the steel bars have just yielded but are not broken (shown in Fig. 11(c)). However, under the unfavorable conditions, some of the steel bars have been broken (shown in Fig. 11(e)) and the barrier is about to tip over (shown in Fig. 12(e)).

When reinforced with vertical reinforcement of ⌀25@200, the three barriers have not overturned. The reinforcement has just yielded but has not been broken under the unfavorable condition. This indicates that the barriers with the reinforcement of ⌀25@200 have better anti-collision resistance.

Fig. 12 shows that the constraint on both ends of barriers has a greater impact on the stress of the reinforcement than the connection between the superstructure and foundation. The

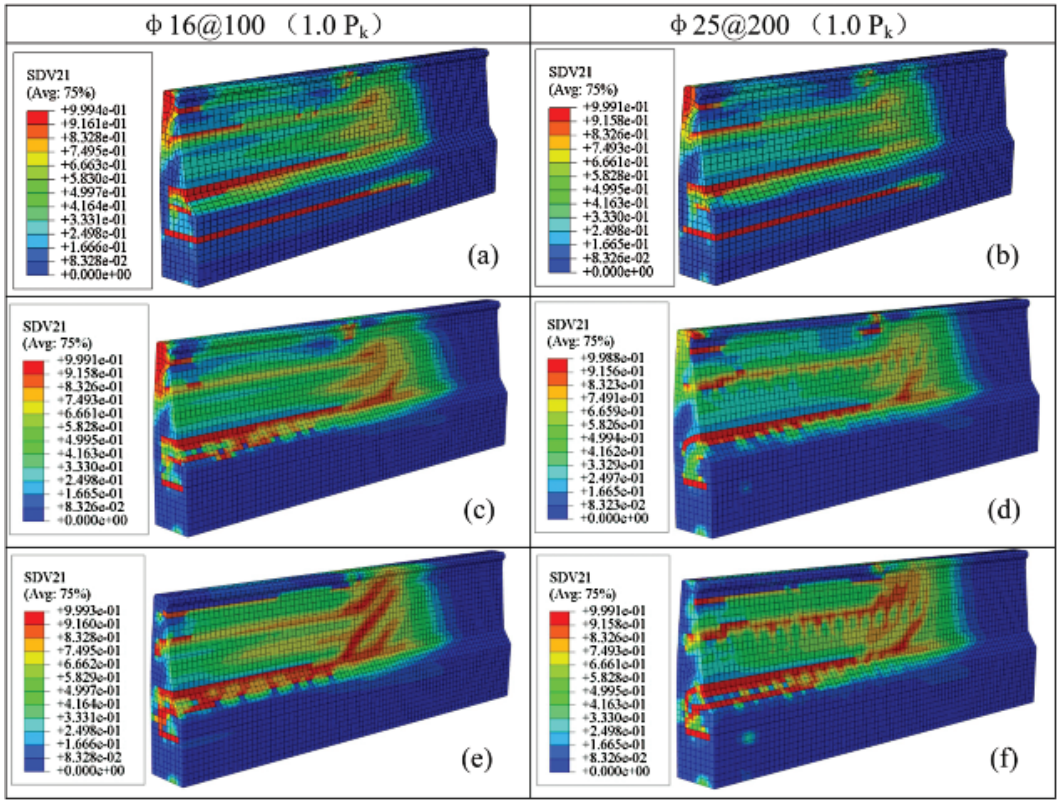

Figure 9: Tensile damage contours of concrete under a corner impact of 1.0 P_k (a) merge-hinge, (b) merge-hinge, (c) tie-hinge, (d) tie-hinge, (e) tie-free, (f) tie-free

reason is that the resistance moment provided by the end constraint is sufficiently large to prevent the barrier from overturning.

4.3 Conditions with an impact load of 1.8 P_k

4.3.1 Central impact

The tensile damage contours of the concrete subjected to a central impact of 1.8 P_k (936 kN) are shown in Fig. 13. Under all the three boundary conditions, the barriers have not overturned and all meet the safety requirements. The barriers with vertical reinforcement of ⌀25@200 have less stress of reinforcement and less tensile damage of the concrete those with vertical reinforcement of ⌀16@100.

4.3.2 Corner impact

The stress contours of the steel bars and the tensile damage contours of the concrete subjected to a corner impact of 1.8 P_k (936 kN) under different constraint conditions are shown in Figs. 14 and 15, respectively. The three barriers with vertical reinforcement of

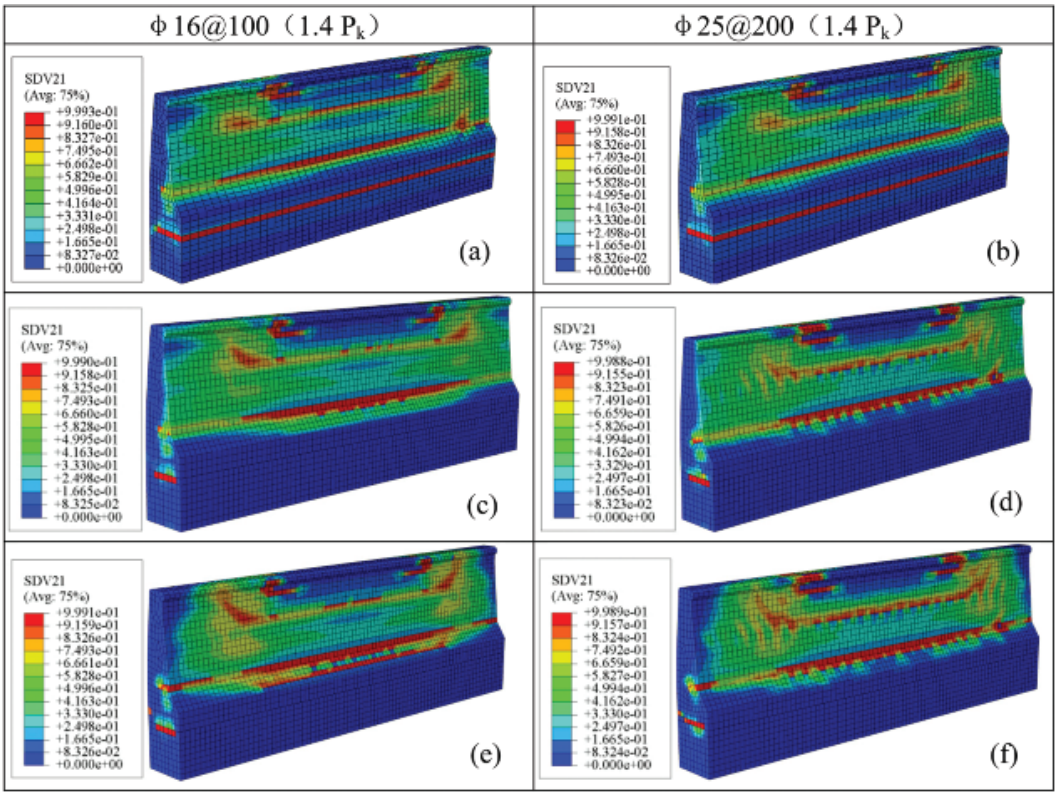

Figure 10: Tensile damage contours of concrete under a central impact of 1.4 P_k (a) merge-hinge, (b) merge-hinge, (c) tie-hinge, (d) tie-hinge, (e) tie-free, (f) tie-free

⌀16@100 have overturned. The overall stress of reinforcement is smaller and the tensile damage of the concrete is less for the reinforcement of ⌀25@200 than that of ⌀16@200 under the same boundary conditions. However, it is only under the ideal condition that the steel bars do not break and the barrier does not overturn (shown in Fig. 14(b)), whereas the barriers overturn under the two other conditions.

4.4 Stress-strain curves under different conditions

4.4.1 Central Impact

When the barrier is subjected to central impact, the stress-strain curves under constraint boundary conditions are shown in Fig. 16, where "16" and "25" stands for the vertical reinforcement of the barrier is ⌀16@100 and ⌀25@200, respectively, and "m-h", "t-h" and "t-f" is the merge-hinge constraint, tie-hinge constraint and tie-free constraint, respectively. Fig. 16 shows that the stress of reinforcement of ⌀25@200 is smaller than that of ⌀16@200 under the same boundary conditions.

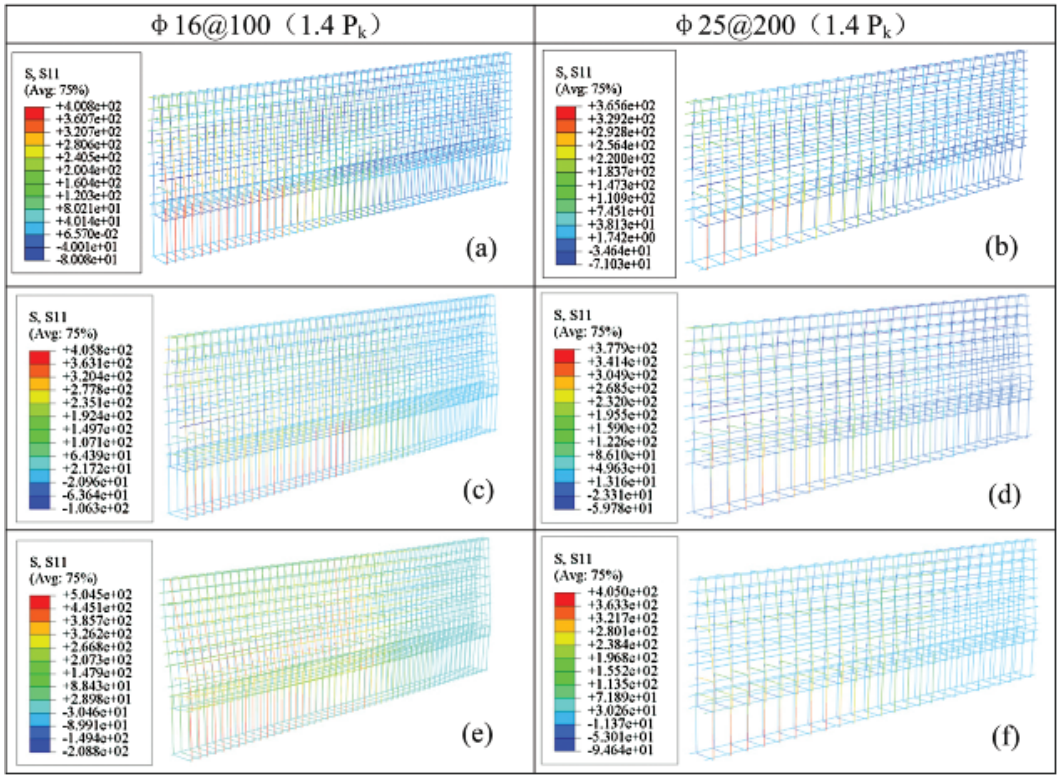

Figure 11: Stress contours of the steel bars under a corner impact of 1.4 P_k (a) merge-hinge, (b) merge-hinge, (c) tie-hinge, (d) tie-hinge, (e) tie-free, (f) tie-free

When the barrier is subjected to a central impact of 1.0 P_k (shown in Fig. 16(a)), the constraints at both ends of the barrier have less of influence on the stress state of the steel bars than the connection between the superstructure and foundation. This is because the longitudinal deformation at both ends of the barrier is small. Through comparison between Figs. 16(a) and 16(b), it can be seen that with the increase of impact load, the difference of influence gradually decreases. When the impact load rise to 1.8 P_k (shown in Fig. 16(c)), the two have a similar impact on the stress of the reinforcement. In addition, none of the steel bars of the barriers have yielded under central impact.

4.4.2 Corner impact

Fig. 17 shows the stress-strain curves when the barrier is subjected to corner impact. Fig. 17(a) shows that none of the steel bars of the barriers have yielded when the impact load is 1.0 P_k. And the connection between the superstructure and foundation has a similar impact on the stress of the reinforcement as the constraint on both ends of the barriers under the same load conditions. But when the impact load rise to 1.4 P_k (shown in Fig. 17(b)), the latter has a greater impact than the former.

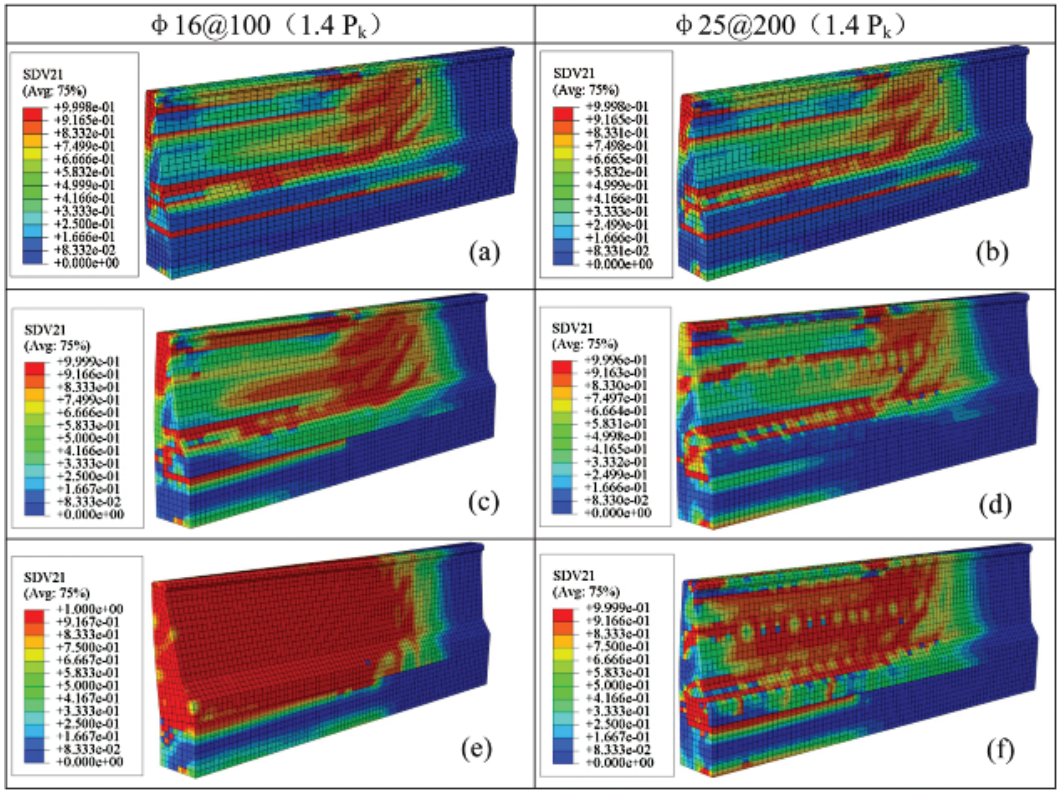

Figure 12: Tensile damage contours of concrete under a corner impact of 1.4 P_k (a) merge-hinge, (b) merge-hinge, (c) tie-hinge, (d) tie-hinge, (e) tie-free, (f) tie-free

In order to more intuitively compare the influence of different constraint conditions on the stress of reinforcement, Fig. 17(b) only shows the stress-strain curves before the stress exceeds the yield stress. Actually, when under the condition of "16-t-f", the barrier is about to tip over for some of the steel bars have been broken as shown in Fig. 11(e). The simulated results clearly indicate that the barriers with the reinforcement of ⌀25@200 have better anti-collision resistance.

5 Conversion of impact load and energy

5.1 Conversion relation

The impact process between a vehicle and the concrete barriers is depicted in Fig. 18. Referring to the reference [JTG D81-2017], a simplified mathematical model of the impact process is established based on the following assumptions.

(1) The longitudinal and transverse acceleration of the vehicle do not change during the collision. The longitudinal direction is the direction along the length of the road and the transverse direction is the direction along the width of the road;

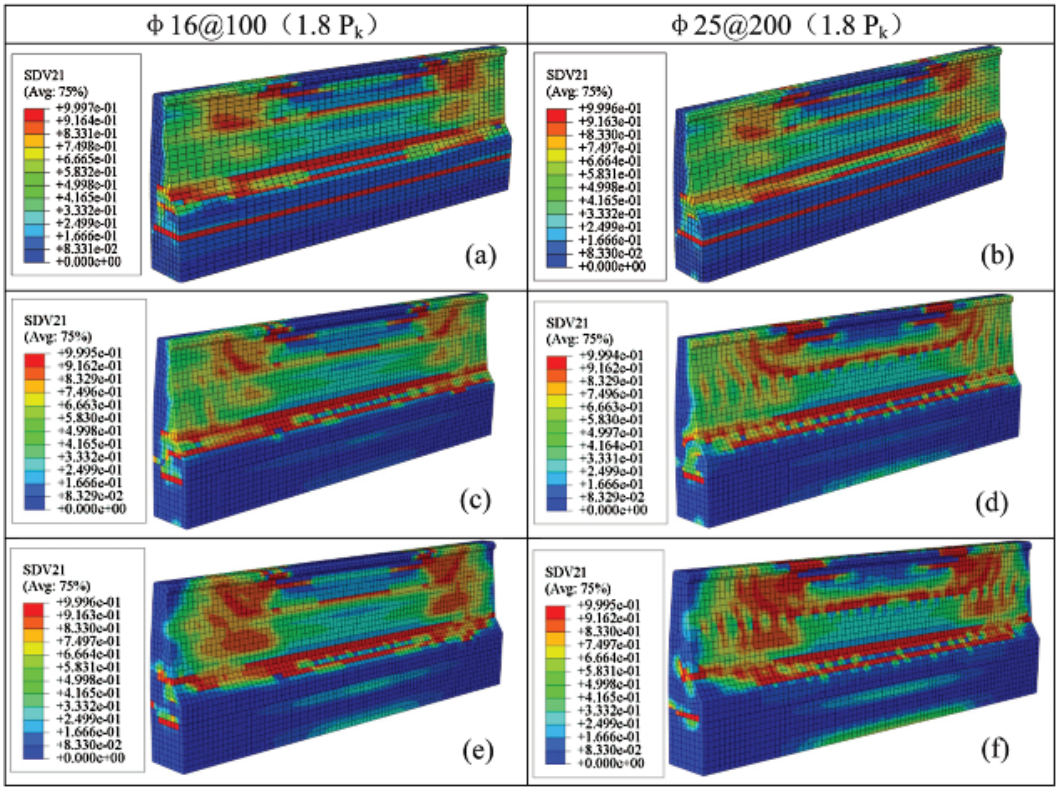

Figure 13: Tensile damage contours of concrete under a central impact of 1.8 P_k (a) merge-hinge, (b) merge-hinge, (c) tie-hinge, (d) tie-hinge, (e) tie-free, (f) tie-free

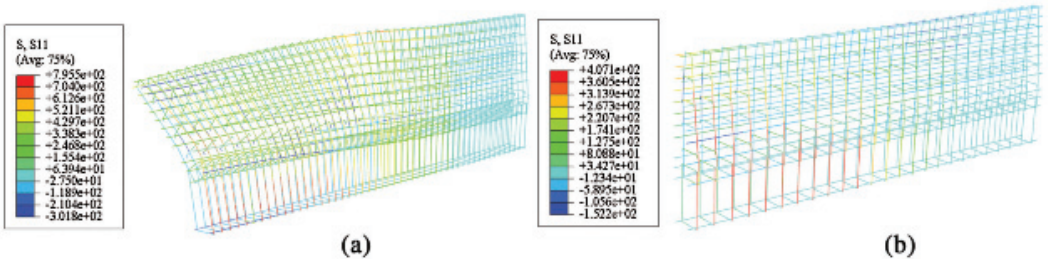

Figure 14: Stress contours of the steel bars under a corner impact of 1.8 P_k. (a) merge-hinge for ⌀16@100 (b) merge-hinge for ⌀25@200

(2) The longitudinal acceleration and rotational acceleration of the vehicle are ignored;

(3) When the vehicle is parallel to the undeformed barrier after the collision, the transverse velocity component of the vehicle is zero;

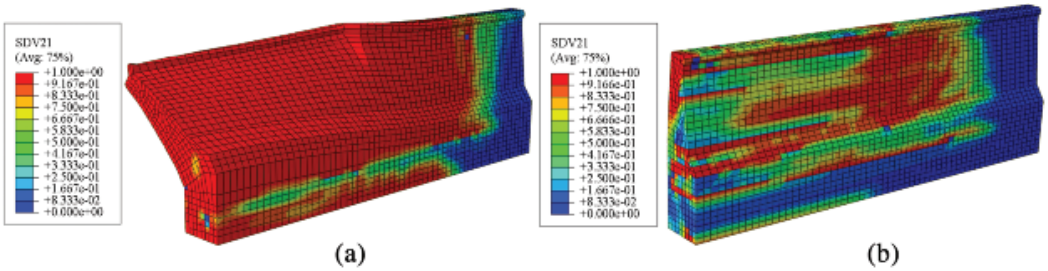

Figure 15: Tensile damage contours of concrete under a corner impact of 1.8 P_k. (a) merge-hinge for ⌀16@100 (b) merge-hinge for ⌀25@200

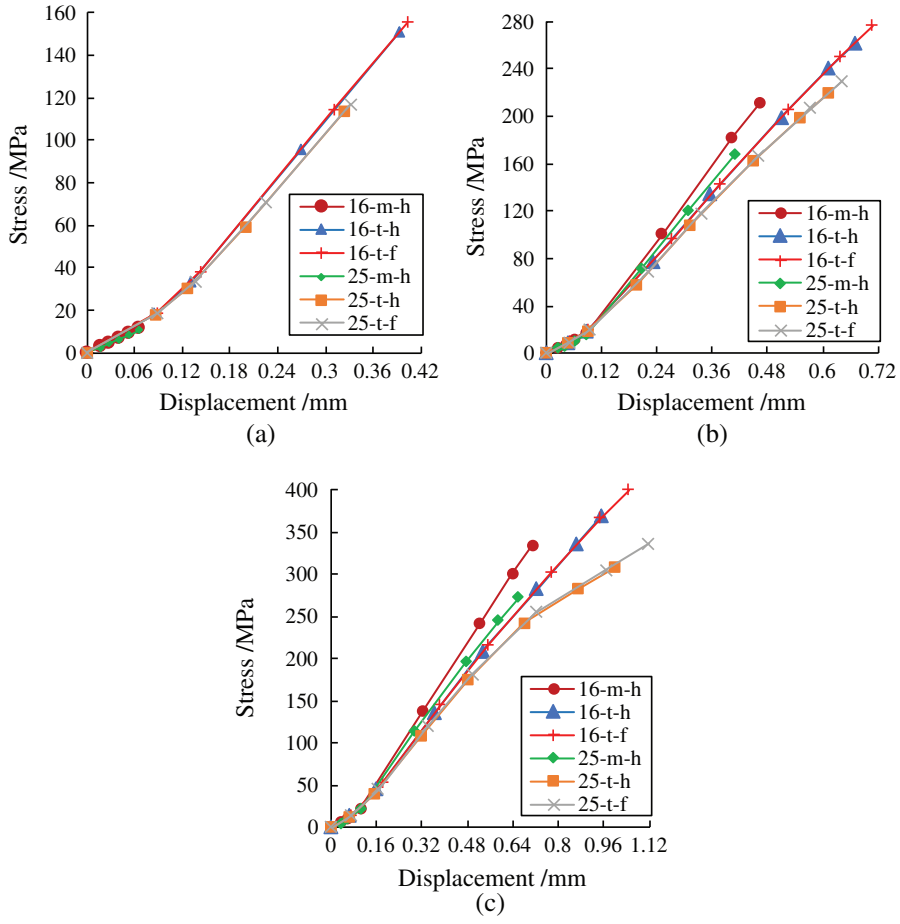

Figure 16: Stress-strain curves under central impact. a) Central impact of 1.0 P_k b) Central impact of 1.4 P_k c) Central impact of 1.8 P_k

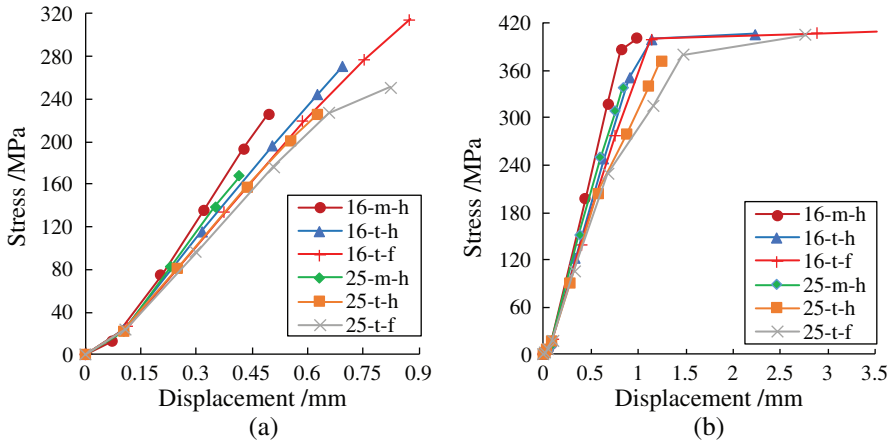

Figure 17: Stress-strain curves under corner impact. a) Central impact of 1.0 P_k b) Central impact of 1.4 P_k

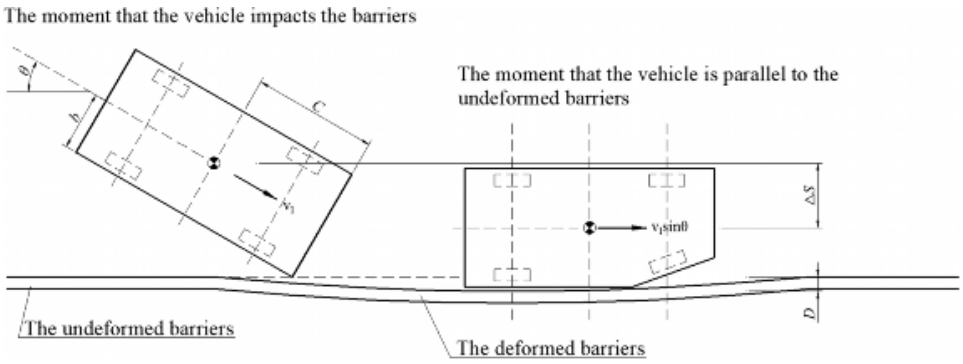

Figure 18: Impact process between vehicle and barriers

(4) The vehicle is allowed to deform during the collision but the position of the vehicle's center of gravity remains unchanged;

(5) Friction between the vehicle and the barriers, as well as between the wheels and road surface is ignored.

As shown in Fig. 18, from the moment when the vehicle collides with the barrier to the moment when the vehicle is parallel to the undeformed barrier, the transverse displacement of the vehicle and the average speed when the vehicle is laterally displaced are expressed by Eqs. (11) and (12), respectively.

$$\Delta S = C\sin\theta - b(1-\cos\theta) + D \tag{11}$$

$$\bar{v}=\frac{1}{2}(v_1 \sin\theta+0)=\frac{1}{2}v_1 \sin\theta \tag{12}$$

where C (m) is the distance between the center of gravity of the vehicle and the front bumper; $\theta(^\circ)$ is the collision angle of the vehicle; b (m) is half the width of the vehicle; D (m) is the maximum transverse dynamic deformation value of the barrier, where D=0 for the concrete barrier; v_1 (m/s) is the collision speed of the vehicle.

According to Eqs. (11) and (12), the time required for the vehicle transverse is defined as:

$$\Delta t=\frac{\Delta S}{\bar{v}}=\frac{2[C\sin\theta-b(1-\cos\theta)+D]}{v_1 \sin\theta} \tag{13}$$

According to Eqs. (12) and (13), the average transverse acceleration of the vehicle can be calculated:

$$a=\frac{v_1 \sin\theta-0}{\Delta t}=\frac{v_1^2 \sin^2\theta}{2[C\sin\theta-b(1-\cos\theta)+D]} \tag{14}$$

When the transverse average acceleration of the vehicle is known, the average transverse force of the vehicle acting on the barrier can be obtained based on Newton's second law:

$$F=ma=\frac{mv_1^2 \sin^2\theta}{2[C\sin\theta-b(1-\cos\theta)+D]} \tag{15}$$

where m is the mass of the vehicle (kg).

The kinetic energy of the vehicle changes due to the resisting effect of the barrier when the vehicle hits the barrier. Based on the kinetic energy theorem, the energy during the collision is defined as:

$$E=\frac{1}{2}m(\Delta v)^2=\frac{1}{2}mv_1^2 \sin^2\theta=F\cdot\Delta S \tag{16}$$

According to Eq. (16), the correlation between the impact energy and the average transverse force during the collision can be established. When the vehicle impacts the barrier, an energy input occurs and the impact energy can be converted into the impact load using Eq. (16). By using this transformation, the stress analysis of the FE model does not only conform to the actual stress state but the complexity of modeling is also greatly reduced.

5.2 Comparison between the calculated and simulated conversion results

According to the law of energy conservation, the kinetic energy lost by the vehicle is equivalent to the impact energy sustained by the barrier. In addition, it is assumed that during the crash process, the barrier can reduce the transverse velocity component of the vehicle to 0 and does not affect the longitudinal velocity component of the vehicle. And

according to the force balance, the mean of the transverse force of the barrier on the vehicle is equal to the average impact load of the vehicle on the barrier. As described in Section 5.1, although the collision is essentially a process of energy input, the mathematical model is used to convert the energy input into a load input, which greatly reduces the complexity of numerical modeling.

In addition, according to the vehicle's physical geometric parameters (m, C, b) and the collision angle (20°) determined by the reference [JTG B05-01-2013] and the standard value of the impact load (520 kN) of the SS-grade concrete barrier, the collision speed of the vehicle and the kinetic energy lost by the vehicle during the collision can be obtained by Eqs. (5) and (6). Take the most common types of passenger cars on the expressway for examples. If the vehicle is an A-class medium-sized passenger car, m is 10800 kg, C is 2.14 m, b is 1.105 m, and the calculated input energy is 345.95 kJ; if the vehicle is a B-class medium-sized passenger car, m is 16950 kg, C is 2.52 m, b is 1.22 m, and the calculated input energy is 409.92 kJ. When the FE model of the precast barrier established in this research uses an impact load of 520 kN, the absorption energy of the barrier with the reinforcements of ⌀16@100 and ⌀25@200 is 378.77 kJ and 364.21 kJ, respectively. The simulation results are close to the calculated values (Eq. (6)) of the medium-sized vehicle. This demonstrates that the proposed FE model accurately simulates the stress state of the concrete barrier during a vehicle collision.

6 Conclusions and recommendations

In this study, a new type of SS-grade precast concrete barrier was designed and a refined FE model considering the stochastic damage-plasticity model of concrete was established using ABAQUS software to investigate the designed parameters of the barrier. The impact load, vertical reinforcement configuration, boundary and constraint conditions were the variables of interest; numerical simulations of the barrier under different working conditions were conducted and the following conclusions were obtained.

(1) The precast concrete barrier with vertical reinforcement of ⌀16@100 can meet the requirements of the Chinese code under impact loads of 1.0 P_k (520 kN) and 1.4 P_k (728 kN) only for the merge-hinge and tie-hinge constraints. For the other constraints, the reinforcement yielded and even broke under certain conditions.

(2) The precast concrete barrier had better mechanical performance when reinforced with vertical reinforcement of ⌀25@200. The vertical reinforcement did not yield and the dynamic response of the barrier met the safety requirements under the impact load of 1.4 P_k (728 kN). Under an impact load of 1.8 P_k (936 kN), the vertical reinforcement yielded and the barrier did not overturn under the ideal constraint conditions. Under the other two conditions, the barrier system had the potential to tip over.

(3) According to the simulated results, it is recommended that the bottom surface of the precast barrier component and the foundation should be connected with mortar with slightly higher strength grade to improve the mechanical performance of the precast barrier under the extreme load of a vehicle. The longitudinal ends of the precast barriers

should set hinged connections and some oblique reinforcing bars should be added in the post-casting area and the foundation to strengthen the connection between the superstructure and foundation.

Funding Statement: This work was supported by the Green Science Architecture Industry Development Co., Ltd., Guizhou, 551400, China. XL Gao received the grant, http://www.gzslzkj.com.

Conflicts of Interest: The authors declare that they have no conflicts of interest to report regarding the present study.

References

Ahmed, E. A.; Dulude, C.; Benmokrane, B. (2013): Concrete bridge barriers reinforced with glass fibre-reinforced polymer: static tests and pendulum impacts. *Canadian Journal of Civil Engineering*, vol. 40, no. 11, pp. 1050-1059. DOI 10.1139/cjce-2013-0019.

Atahan, A. O. (2006): Finite-element crash test simulation of new york portable concrete barrier with I-shaped connector. *Journal of Structural Engineering*, vol. 132, no. 3, pp. 430-440. DOI 10.1061/(ASCE)0733-9445(2006)132:3(430).

Atahan, A. O. (2009): Effect of permanent jersey-shaped concrete barrier height on heavy vehicle post-impact stability. *International Journal of Heavy Vehicle Systems*, vol. 16, no. 1, pp. 243-257. DOI 10.1504/IJHVS.2009.023863.

Atahan, A. O.; Cansiz, Ö. F. (2005): Improvements to G4 (RW) strong-post round-wood, W-beam guardrail system. *Journal of Transportation Engineering*, vol. 131, no. 1, pp. 63-73. DOI 10.1061/(ASCE)0733-947X(2005)131:1(63).

Bielenberg, R. W.; Faller, R. K.; Reid, J. D.; Schmidt, J. D.; Asadollahi Pajouh, M. et al. (2018): Development of retrofit, low-deflection portable concrete barrier system. *Journal of Transportation Safety & Security*, vol. 11, no. 4, pp. 333-352.

Bligh, R. P.; Sheikh, N. M.; Menges, W. L.; Haug, R. R. (2005): Development of low-deflection precast concrete barrier. *Report No. FHWA/TX-05/0-4162-3, Texas Transportation Institute, Texas A & M University, College Station, TX*.

Borkowski, W.; Hryciów, Z.; Rybak, P.; Wysocki, J. (2010): Numerical simulation of the standard TB11 and TB32 tests for a concrete safety barrier. *Journal of KONES*, vol. 17, no. 4, pp. 63-71.

Borkowski, W.; Hryciów, Z.; Rybak, P.; Wysocki, J. (2011): Prototype articulated joint in connections of the concrete protective barrier. *Journal of KONES*, vol. 18, no. 1, pp. 85-92.

Consolazio, G. R.; Chung, J. H.; Gurley, K. R. (2003): Impact simulation and full scale crash testing of a low profile concrete work zone barrier. *Computers & Structures*, vol. 81, no. 13, pp. 1359-1374. DOI 10.1016/S0045-7949(03)00058-0.

Deb, A.; Naravane, A.; Chirwa, E. C. (2006): An offset rigid barrier-based test: equivalence to the insurance institute for highway safety frontal offset impact safety test.

International Journal of Crashworthiness, vol. 11, no. 4, pp. 281-290. DOI 10.1533/ijcr.2005.0407.

Faller, R. K.; Reid, J. D.; Kretschmann, D. E.; Hascall, J. A.; Sicking, D. L. (2009): Midwest guardrail system with round timber posts. *Transportation Research Record*, vol. 2120, no. 1, pp. 47-59. DOI 10.3141/2120-06.

Faller, R. K.; Sicking, D. L.; Bielenberg, R. W.; Rohde, J. R.; Polivka, K. A. et al. (2007): Performance of steel-post, W-beam guardrail systems. *Transportation Research Record*, vol. 2025, no. 1, pp. 18-33. DOI 10.3141/2025-02.

Feng, D. C.; Yang, C. D.; Ren, X. D. (2018): Multi-scale stochastic damage model for concrete and its application to RC shear wall structure. *Engineering Computations*, vol. 35, no. 6, pp. 2287-2307.

Hála, P.; Sovják, R.; Frydrýn, M.; Mičunek, T. (2017): Energy absorbing system made of high performance concrete. *Construction and Building Materials*, vol. 139, pp. 64-80. DOI 10.1016/j.conbuildmat.2017.02.048.

Hou, S. J.; Zheng, Y.; Xie, J.; Han, X. U. (2014): Optimization design of NJ shaped guardrail based on collision safety consideration. *International Journal of Computational Methods*, vol. 11, no. 6, pp. 63-83. DOI 10.1142/S0219876213500837.

Itoh, Y.; Liu, C.; Kusama, R. (2007): Dynamic simulation of collisions of heavy high-speed trucks with concrete barriers. *Chaos Solitons & Fractals*, vol. 34, no. 4, pp. 1239-1244. DOI 10.1016/j.chaos.2006.05.059.

Janda, T.; Zemanová, A.; Hála, P.; Konrád, P.; Schmidt, J. (2020): Reduced order model of glass plate loaded by low-velocity impact. *International Journal of Computational Methods and Experimental Measurements*, vol. 8, no. 1, pp. 36-46. DOI 10.2495/CMEM-V8-N1-36-46.

Jeon, S. J.; Choi, M. S.; Kim, Y. J. (2008): Ultimate strength of concrete barrier by the yield line theory. *International Journal of Concrete Structures and Materials*, vol. 2, no. 1, pp. 57-62. DOI 10.4334/IJCSM.2008.2.1.057.

Jiang, T.; Grzebieta, R. H.; Zhao, X. L. (2004): Predicting impact loads of a car crashing into a concrete roadside safety barrier. *International Journal of Crashworthiness*, vol. 9, no. 1, pp. 45-63. DOI 10.1533/ijcr.2004.0271.

JTG B05-01-2013 (2013): *Standard for Safety Performance Evaluation of Highway Barriers*.

JTG D81-2017 (2017): *Design Specifications for Highway Safety Facilities*.

JTG/T D81-2017 (2017): *Design Guidelines for Highway Safety Facilities*.

Kim, W.; Lee, I.; Kim, K.; Jeong, Y.; Lee, J. (2019): Evaluation of concrete barriers with novel shock absorbers subjected to impact loading. *Archives of Civil and Mechanical Engineering*, vol. 19, no. 3, pp. 657-671. DOI 10.1016/j.acme.2019.01.004.

Kusama, R. (2004). *Study on Numerical Collision Analysis for Performance-Based Design of Guard Fences*. *Master Thesis*. Department of Civil Engineering, Nagoya University, Nagoya, Japan.

Lai, X.; Ren, B.; Fan, H.; Li, S.; Wu, C. T. et al. (2015): Peridynamics simulations of geomaterial fragmentation by impulse loads. *International Journal for Numerical and Analytical Methods in Geomechanics*, vol. 39, no. 12, pp. 1304-1330. DOI 10.1002/nag.2356.

Li, J.; Feng, D. C.; Ren, X. D.; Wan, Z. Y. (2017): Calibration and application of concrete stochastic damage model. *Chinese Journal of Tongji University (Natural Science)*, vol. 45, no. 8, pp. 1099-1107.

Li, S.; Liu, W. K. (2002): Meshfree and particle methods and their applications. *Applied Mechanics Reviews*, vol. 55, no. 1, pp. 1-34. DOI 10.1115/1.1431547.

Li, J.; Ren, X. D. (2009): Stochastic damage model for concrete based on energy equivalent strain. *International Journal of Solids and Structures*, vol. 46, no. 11-12, pp. 2407-2419. DOI 10.1016/j.ijsolstr.2009.01.024.

Liang, J. S.; Ren, X. D.; Li, J. (2015): A competitive mechanism driven damage-plasticity model for fatigue behavior of concrete. *International Journal of Damage Mechanics*, vol. 25, no. 3, pp. 377-399. DOI 10.1177/1056789515586839.

Ma, Z. Q.; Kong, L. S.; Jin, X. L. (2018): An explicit-implicit mixed staggered asynchronous step integration algorithm in structural dynamics. *Computer Modeling in Engineering & Sciences*, vol. 116, no. 1, pp. 51-67. DOI 10.31614/cmes.2018.01739.

Marzougui, D.; Kan, C. D.; Opiela, K. (2012): Safety performance evaluation of concrete barriers on curved and superelevated roads. *Transportation Research Board Annual Meeting*, vol. 83, no. 3, pp. 446-456.

Mohammed, H. J.; Zain, M. F. M. (2016): Experimental application of EPS concrete in the new prototype design of the concrete barrier. *Construction and Building Materials*, vol. 124, pp. 312-342. DOI 10.1016/j.conbuildmat.2016.07.105.

Pachocki, Ł.; Wilde, K. (2018): Numerical simulation of the influence of the selected factors on the performance of a concrete road barrier H2/W5/B. *MATEC Web of Conferences*, vol. 231, pp. 01014.

Reid, J. D.; Sicking, D. L.; Faller, R. K.; Pfeifer, B. G. (1997): Development of a new guardrail system. *Transportation Research Record*, vol. 1599, no. 1, pp. 72-80. DOI 10.3141/1599-09.

Ren, X. D.; Liu, K.; Li, J.; Gao, X. L. (2017): Compressive behavior of stirrup-confined concrete under dynamic loading. *Construction & Building Materials*, vol. 154, pp. 10-22. DOI 10.1016/j.conbuildmat.2017.07.174.

Ren, Z.; Vesenjak, M. (2005): Computational and experimental crash analysis of the road safety barrier. *Engineering Failure Analysis*, vol. 12, no. 6, pp. 963-973. DOI 10.1016/j.engfailanal.2004.12.033.

Ren, X. D.; Zeng, S. J.; Li, J. (2015): A rate-dependent stochastic damage-plasticity model for quasi-brittle materials. *Computational Mechanics*, vol. 55, no. 2, pp. 267-285. DOI 10.1007/s00466-014-1100-7.

Ross, H. E.; Sicking, D. L.; Zimmer, R. A.; Michie, J. D. (1993): NCHRP report 350: recommended procedures for the safety performance evaluation of highway features. *TRB, National Research Council*, Washington, DC.

Sennah, K.; Hedjazi, S. (2019): Structural qualification of a developed GFRP-reinforced TL-5 concrete bridge barrier using vehicle crash testing. *International Journal of Crashworthiness*, vol. 24, no. 3, pp. 296-313. DOI 10.1080/13588265.2018.1480582.

Sicking, D. L.; Reid, J. D.; Rohde, J. R. (2002): Development of the Midwest Guardrail system. *Transportation Research Record*, vol. 1797, no. 1, pp. 44-52. DOI 10.3141/1797-06.

Soltani, M.; Moghaddam, T. B.; Karim, M. R.; Sulong, N. H. R. (2013): The safety performance of guardrail systems: review and analysis of crash tests data. *International Journal of Crashworthiness*, vol. 18, no. 5, pp. 530-543. DOI 10.1080/13588265.2013.815020.

Wang, J.; Jiang, W.; Wang, Q. (2019): Numerical simulation and experimental studies on elastic-plastic fatigue crack growth. *Computer Modeling in Engineering & Sciences*, vol. 118, no. 2, pp. 377-395. DOI 10.31614/cmes.2019.01836.

Yin, H.; Fang, H.; Wang, Q.; Wen, G. (2016): Design optimization of a MASH TL-3 concrete barrier using RBF-based metamodels and nonlinear finite element simulations. *Engineering Structures*, vol. 114, pp. 122-134. DOI 10.1016/j.engstruct.2016.02.009.

Zhao, J.; Lei, Z. B.; Wang, S. J.; Li, Y. H.; Lei, M. X. (2011): Optimization of the level of SS crash barrier overpass bridge on highway. *Second International Conference on Mechanic Automation & Control Engineering*, pp. 2346-2349.